

INSIGHT: Explainable Weakly-Supervised Medical Image Analysis

Wenbo Zhang
University of Rochester

Junyu Chen
University of Rochester

Christopher Kanan
University of Rochester

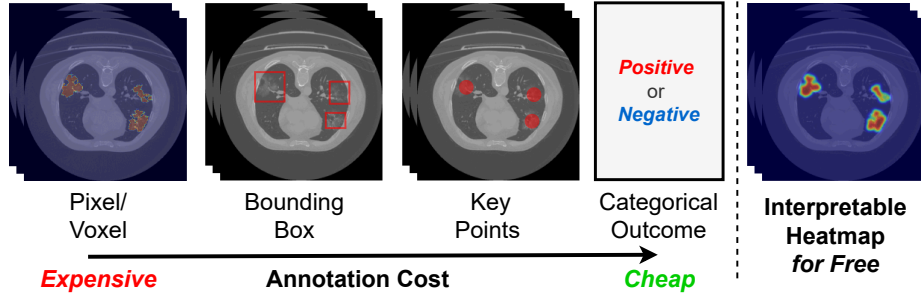


Figure 1. Semantic segmentation for medical data often requires expensive annotations that are not done routinely in clinical practice, whereas INSIGHT only needs image-level labels (left). Unlike other weakly-labeled methods, INSIGHT has per-label heatmaps built into the architecture as a form of inductive bias, enabling it to directly produce heatmaps that closely align with ground-truth diagnostic regions *without* the use of post-hoc methods like Grad-CAM (right).

Abstract

Due to their large sizes, volumetric scans and whole-slide pathology images (WSIs) are often processed by extracting embeddings from local regions and then an aggregator makes predictions from this set. However, current methods require post-hoc visualization techniques (e.g., Grad-CAM) and often fail to localize small yet clinically crucial details. To address these limitations, we introduce INSIGHT, a novel weakly-supervised aggregator that integrates heatmap generation as an inductive bias. Starting from pre-trained feature maps, INSIGHT employs a detection module with small convolutional kernels to capture fine details and a context module with a broader receptive field to suppress local false positives. The resulting internal heatmap highlights diagnostically relevant regions. On CT and WSI benchmarks, INSIGHT achieves state-of-the-art classification results and high weakly-labeled semantic segmentation performance. Project website and code are available at: <https://zhangdylan83.github.io/ewsmia/>

1. Introduction

Advances in medical imaging technology have enabled clinicians to extract critical insights from increasingly large and complex datasets. However, the size of medical images presents computational and analytical challenges: whole-

slide images (WSIs) of histopathology slides can contain billions of pixels [3], and volumetric scans, such as CT or MRI, are composed of hundreds of slices. Processing such data end-to-end with deep neural networks is computationally infeasible. Instead, pipelines rely on aggregators, which synthesize local embeddings extracted from tiles (WSIs) or slices (volumes) into global predictions [5, 6, 23]. While this divide-and-conquer strategy is efficient, current methods often discard spatial information during feature aggregation and depend on post-hoc visualization tools, such as Grad-CAM [33], to generate interpretable heatmaps. These visualizations are prone to missing clinically significant features and introduce additional complexity.

To address these limitations, we propose **INSIGHT** (Integrated Network for Segmentation and Interpretation with Generalized Heatmap Transmission), a novel weakly-supervised aggregator that embeds interpretability directly into its architecture. INSIGHT processes pre-trained patch- or slice-level embeddings through two complementary modules: a *Detection Module*, which captures fine-grained diagnostic features, and a *Context Module*, which suppresses irrelevant activations by incorporating broader spatial information. These outputs are fused to create interpretable *internal* heatmaps that naturally align with diagnostic regions. INSIGHT produces internal segmentation-quality heatmaps without requiring pixel- or voxel-level annotations as shown in Fig. 1.

Weak supervision is essential in medical imaging, where the creation of detailed annotations is expensive and labor-intensive [3]. Fully supervised methods like U-Net [31] and DeepLab [7] rely on densely labeled data, which limits their scalability. In contrast, multiple instance learning (MIL) [3, 4] enables models to aggregate features from local regions using only image- or slide-level labels, avoiding the need for pixel-level annotations. This approach allows models to train on significantly larger datasets, as physicians typically diagnose patients without annotating individual image regions. For instance, the FDA-cleared Paige Prostate system demonstrates the clinical viability of weak supervision by achieving high diagnostic accuracy for prostate cancer detection [3, 46]. Similarly, MIL-based methods have effectively aggregated patch- or slice-level features to make predictions on WSIs and volumetric scans [5, 6].

However, current weakly supervised methods face critical limitations. They require post-hoc visualization techniques, such as Grad-CAM [33] or class activation maps (CAM) [45], to produce interpretable saliency maps, adding complexity and often failing to localize small yet clinically essential details. These saliency maps can also be biased by dataset characteristics, such as organ co-occurrence, and often struggle to balance classification accuracy with spatial localization [10]. This leaves considerable room for improvement in designing aggregators that can better capture spatial dependencies and produce clinically meaningful outputs. INSIGHT addresses these challenges by directly embedding interpretability into its architecture, eliminating the reliance on post-hoc methods and bridging the gap between computational efficiency and clinical relevance.

This paper makes the following contributions:

- We introduce INSIGHT, a novel weakly-supervised aggregator that directly integrates explainability into its architecture, producing high-quality heatmaps as part of its decision-making process.
- We demonstrate that INSIGHT achieves state-of-the-art performance on three challenging medical imaging datasets, excelling in both classification and segmentation tasks across CT and WSI modalities.
- Through extensive qualitative and quantitative analyses, we show that INSIGHT’s heatmaps align closely with diagnostic regions, requiring only image-level labels for supervision.

2. Related Work

2.1. Weakly Supervised Medical Image Learning

Fully supervised methods such as U-Net [31] and DeepLab [7] have achieved high segmentation accuracy in medical imaging. However, their reliance on dense, pixel- or voxel-level annotations limits scalability in clinical work-

flows [3]. Weakly supervised learning mitigates this issue by enabling models to train on coarser annotations, such as image- or slide-level labels, which are more practical in large-scale clinical datasets.

Methods based on MIL have proven effective for WSIs and volumetric data, where detailed annotations are unavailable. MIL aggregates features from local patches or slices to predict global outcomes, bypassing the need for pixel-level labels. For example, the FDA-cleared Paige Prostate system demonstrated the clinical viability of MIL by achieving high diagnostic accuracy for prostate cancer detection using only slide-level labels [3, 46]. MIL-based methods have also been successfully applied to breast cancer subtyping from WSIs [5] and chemotherapy response prediction from volumetric CT scans [6].

While alternative weak labeling strategies, such as scribbles [19], bounding boxes [20], or point-level markers [16], reduce annotation demands, they still require explicit region annotations, which are rarely performed by physicians in clinical practice. INSIGHT builds on the MIL paradigm by utilizing only image-level labels for both classification and segmentation. Unlike existing methods, INSIGHT incorporates interpretability directly into its architecture, generating fine-grained heatmaps that align with diagnostic regions without requiring post-hoc visualization techniques.

2.2. Aggregation Techniques in Medical Imaging

Aggregation techniques are essential for efficiently processing large-scale medical imaging data, such as WSIs and volumetric scans, without requiring dense annotations. In WSIs, MIL-based methods treat each slide as a collection of patches and aggregate features for global predictions. For instance, MIL has been successfully applied to cancer detection using slide-level labels [3], while advancements like STAMP [25] and tissue-graph approaches [28] have improved WSI analysis by refining aggregation techniques to detect patterns and segment tissues.

In volumetric imaging, slice-level features are aggregated to form volume-level predictions. For example, multi-resolution systems like [32] use DenseVNet-generated features to improve classification of chest CT scans, while [43] developed an aggregation framework with label correction to enhance outcome predictions.

INSIGHT advances these techniques by preserving spatial resolution across slices or patches until the final pooling stage, enabling the generation of detailed, localized heatmaps. This addresses a key limitation of traditional aggregation methods, which often discard spatial information, reducing their ability to localize diagnostically relevant regions.

2.3. Explainable AI Methods in Medical Imaging

Explainable AI is crucial for ensuring model predictions in medical imaging are interpretable and clinically meaningful. Post-hoc methods such as class activation maps (CAM) [45] and Grad-CAM [33] are widely used to generate saliency maps that highlight regions associated with model predictions. For example, [42] developed high-resolution CAMs for thoracic CT scans, while [40] refined pseudo-labels for chest X-ray segmentation using CAMs.

Attention mechanisms have further advanced interpretability. Self-attention, as introduced in [39], has been combined with Grad-CAM to localize disease-specific regions [44], while dual-attention mechanisms, such as DAMIL [9], produce interpretable maps for detecting conditions like COVID-19 and bacterial pneumonia.

While these methods generate useful insights, they rely on post-hoc interpretability, which can misalign with the model’s decision-making process. INSIGHT eliminates this reliance by embedding interpretability directly into its architecture, producing calibrated, built-in heatmaps as part of its predictions. This ensures alignment between the model’s outputs and diagnostic reasoning.

2.4. Pre-training in Medical Image Analysis

Pre-trained models have significantly advanced medical imaging by providing robust feature extractors. ResNet-based architectures, such as those used in [11, 17], effectively capture local and intermediate features in weakly supervised frameworks. However, CNNs face limitations in capturing long-range dependencies, which are critical for analyzing complex medical images.

Vision Transformers (ViTs) [12] address these limitations by leveraging self-attention to capture broader spatial relationships. INSIGHT leverages pre-trained ViTs to extract tensor embeddings from WSI patches and radiology slices. By preserving spatial resolution, INSIGHT achieves robust performance across WSI and CT datasets, supporting fine-grained analysis and interpretability.

3. Method

Fig. 2 illustrates the architecture of INSIGHT, a weakly supervised framework for medical image analysis. INSIGHT processes pre-trained features from each slice in a volume or each patch in a WSI through dual modules—Detection and Context—to generate fine-grained heatmaps. These heatmaps are aggregated using a SmoothMax pooling strategy to produce categorical predictions, optimized using a combination of binary cross-entropy (BCE) and spectral decoupling losses. Below, we describe each component in detail.

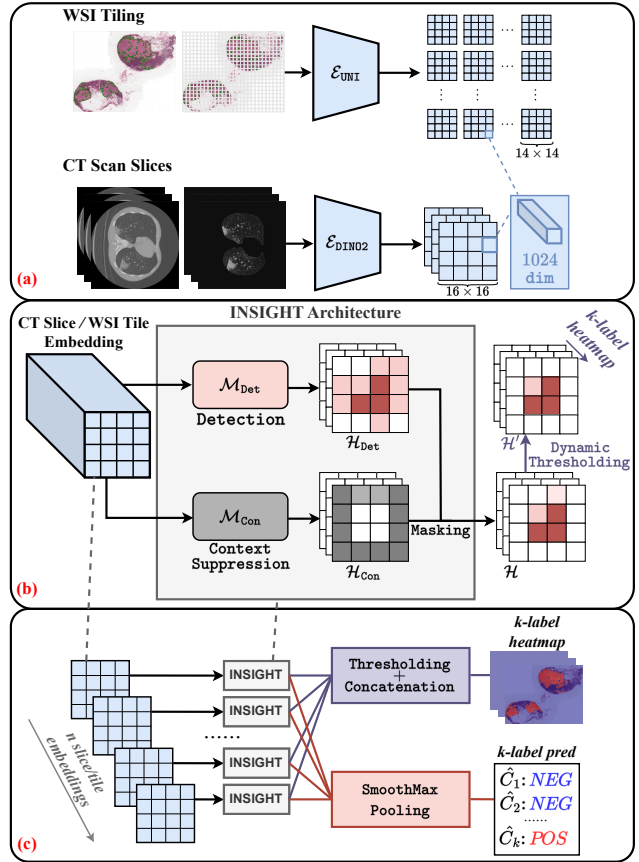


Figure 2. INSIGHT’s inputs and architecture. (a) Images are pre-processed to extract pre-trained features from each CT slice or WSI patch. (b) These features are processed through the Detection and Context modules to generate slice- or patch-level heatmaps by incorporating both fine-grained details and broader contextual information. (c) Heatmaps are aggregated across slices or patches to produce a binary prediction for each category along with interpretable heatmaps.

3.1. Feature Extraction

To preserve spatial resolution and capture both local and global contextual information, INSIGHT uses pre-trained models specific to the input modality. For CT scan volumes, we use a ViT pre-trained with DINOv2 [26] on ImageNet. For pathology WSIs, we use UNI [8], a DINOv2 model pre-trained on over 100 million WSIs. The extracted 2D feature maps are denoted as $F \in \mathbb{R}^{c \times h \times w}$, where c , h , and w are the feature depth, height, and width, respectively.

3.2. INSIGHT Architecture

Feature Adaptation. Pre-trained feature maps are transformed to domain-specific representations via a linear transformation layer:

$$F_t = \mathbf{W}F + \mathbf{b}, \quad (1)$$

where $\mathbf{W} \in \mathbb{R}^{c' \times c}$ and $\mathbf{b} \in \mathbb{R}^{c'}$ adapt the features to the target dataset. The transformed features $F_t \in \mathbb{R}^{c' \times h \times w}$ are then fed into two parallel modules: Detection and Context. **Detection Module.** This module uses small-kernel convolutions to capture fine-grained details such as textures and edges, producing a heatmap \mathcal{H}_{Det} that highlights potential regions of interest:

$$\mathcal{H}_{\text{Det}} = \mathcal{M}_{\text{Det}}(F_t). \quad (2)$$

Context Module. To reduce false positives from the Detection module, the Context module uses large-kernel convolutions to capture broader spatial context and suppress irrelevant activations. Its output, \mathcal{H}_{Con} , acts as a gating mechanism:

$$\mathcal{H}_{\text{Con}} = \mathcal{M}_{\text{Con}}(F_t). \quad (3)$$

Heatmap Fusion. The Detection and Context outputs are combined to generate a refined heatmap:

$$\mathcal{H} = \sigma((1 - \sigma(\mathcal{H}_{\text{Con}})) \odot \mathcal{H}_{\text{Det}}), \quad (4)$$

where σ is the sigmoid activation, and \odot denotes element-wise multiplication. The resulting heatmap \mathcal{H} assigns relevance scores to regions, aligning with the target labels.

3.3. Pooling and Classification

To produce a categorical outcome, heatmaps are aggregated across all slices or patches using SmoothMax pooling [22], a Boltzmann-weighted operator that emphasizes regions with strong activations:

$$\hat{y} = \frac{\sum_i \mathcal{H}_i \cdot \exp(\alpha \cdot \mathcal{H}_i)}{\sum_i \exp(\alpha \cdot \mathcal{H}_i)}, \quad (5)$$

where \hat{y} is the predicted likelihood of a positive outcome, \mathcal{H}_i are heatmap activations, and α controls the weighting. For multi-label classification, the heatmap is extended to multiple channels, one per category, enabling simultaneous optimization for all labels.

3.4. Training Objective

Binary Cross-Entropy with Label Smoothing. BCE loss with label smoothing improves generalization and prevents overconfidence in noisy or overlapping labels:

$$\mathcal{L}_{\text{BCE}} = -\frac{1}{N} \sum_{i=1}^N [y'_i \log(\hat{y}_i) + (1 - y'_i) \log(1 - \hat{y}_i)], \quad (6)$$

where $y'_i = (1 - \epsilon)y_i + \frac{\epsilon}{2}$ is the smoothed label, ϵ is the smoothing factor, and \hat{y}_i is the predicted probability.

Spectral Decoupling. To address gradient starvation and encourage robust decision boundaries, we include spectral decoupling loss [29]:

$$\mathcal{L}_{\text{SD}} = \frac{\lambda_{\text{SD}}}{2} \cdot \|z\|_2^2, \quad (7)$$

where z are unnormalized logits, and λ_{SD} controls regularization strength. Spectral decoupling is one of the most effective methods for overcoming dataset bias without additional sub-group labels [36, 37].

Total Loss. The total loss combines these objectives:

$$\mathcal{L} = \mathcal{L}_{\text{BCE}} + \mathcal{L}_{\text{SD}}. \quad (8)$$

3.5. Heatmap Visualization

Heatmaps are resized and reconstructed to match the original image dimensions. For WSIs, patches are stitched based on coordinates, while for CT volumes, slices are stacked sequentially. Dynamic thresholding with Otsu’s algorithm [27] isolates regions of interest:

$$\mathcal{H}' = \mathcal{H} \cdot \mathbb{I}(\mathcal{H} > T), \quad (9)$$

where $T = \arg \min_t \sigma_w^2(t)$ minimizes intra-class variance.

4. Experiments

4.1. Datasets and Preprocessing

We evaluate INSIGHT on three publicly available datasets representing two imaging modalities: CT volumes and WSIs.

4.1.1. Computed Tomography (CT) Dataset

MosMed [24]. The MosMed dataset comprises 1,110 chest CT studies for COVID-19 detection, split into two subsets: MosMed-A (1,060 volumes) and MosMed-B (50 volumes). MosMed-A is used for classification tasks, employing five-fold cross-validation with an 80/20 train-test split. MosMed-B, containing voxel-level annotations, is used solely for evaluating segmentation performance by comparing INSIGHT-generated heatmaps \mathcal{H} against ground truth using Dice score.

CT volumes are normalized to the Hounsfield Unit (HU) range $[-1000, 400]$, scaled to $[0, 1]$, and resized to $518 \times 518 \times 32$. To ensure compatibility with pre-trained ViTs, single-channel data is replicated across three channels. Lung parenchyma is isolated using Lungmask [14].

4.1.2. Whole Slide Image (WSI) Datasets

CAMELYON16 [18]. This dataset contains 399 WSIs for detecting metastatic breast cancer in lymph nodes. We split the 269 training slides into 90/10 for training and validation. The model checkpoint with the highest validation Dice score is evaluated on the official test set of 129 slides.

BRACS [1]. This dataset contains 547 WSIs annotated with 4,539 bounding boxes for breast carcinoma subtype classification. Following BRACS’s official splits, the final dataset comprises 347, 51, and 73 slides for training, validation, and testing, respectively.

Both CAMELYON16 and BRACS use the CLAM toolbox [21] for patch extraction, preserving spatial embeddings for INSIGHT.

Table 1. Performance comparison on the CAMELYON16 and BRACS official test datasets. ALL aggregators use UNI [8] for embeddings. We report AUC and Dice score (mean \pm std) for CAMELYON16, and AUC scores for different categories in BRACS, with Macro AUC as the overall score. Reported Dice scores for all comparison methods were fine-tuned through grid search on the validation set.

Aggregator	CAMELYON16 [18]		BRACS [1]				
	AUC	Dice(%)	ADH	FEA	DCIS	Invasive	Macro AUC
ABMIL [15]	0.975	55.8 \pm 25.0	0.656	0.744	0.804	0.995	0.800
CLAM-SB [21]	0.966	64.7 \pm 24.1	0.611	<u>0.757</u>	<u>0.833</u>	0.999	0.800
CLAM-MB [21]	0.973	<u>67.7\pm22.6</u>	<u>0.701</u>	<u>0.687</u>	<u>0.828</u>	<u>0.998</u>	<u>0.804</u>
TransMIL [35]	<u>0.982</u>	<u>12.4\pm22.4</u>	0.644	0.653	0.769	0.989	<u>0.764</u>
INSIGHT	0.990	74.6\pm19.1	0.734	0.790	0.837	0.999	0.840

Table 2. Performance comparison for classification and segmentation on the MosMed dataset. Methods marked with * were trained on an external dataset but tested on the same MosMed test set for consistency.

Task	Method	Setting	AUC / Dice(%)
Classification	ViT-COVID [38]	0.6/0.2/0.2 split	0.870
	PR-3D-CNN [13]	Five-fold CV	0.914 \pm 0.049
	INSIGHT	Five-fold CV	0.962 \pm 0.012
Segmentation	3D U-Net [2]*	Voxel-level	40.5 \pm 21.3
	3D GAN [34]	Volume-level	41.2 \pm 14.7
	INSIGHT	Volume-level	42.7 \pm 15.3

4.2. INSIGHT’s Implementation Details

Architecture. INSIGHT uses ViT-L/DINOv2 for CT slices and UNI for WSI tiles. Pre-processed inputs are resized to 224×224 , and embeddings from the last layer of the encoder are concatenated to retain spatial information. Dimensionality is reduced from 1024 to 128 using a linear transformation. Detection and Context modules consist of three convolutional layers with GELU activations, layer normalization, and a final layer for label-specific outputs.

Training Configuration. INSIGHT is trained using AdamW with a learning rate of 10^{-4} and weight decay of 10^{-4} . Training is capped at 50 epochs, with early stopping triggered after 8 epochs of no validation improvement. Hyperparameters, including $\alpha = 8$ for SmoothMax pooling, are tuned on validation sets. Label smoothing is applied for multi-label classification on BRACS, while Spectral Decoupling is used for MosMed and CAMELYON16 to improve generalization.

4.3. Compared Baselines

We compare INSIGHT to several state-of-the-art methods across the MosMed, CAMELYON16, and BRACS datasets, evaluating both classification and segmentation performance.

MosMed. For the MosMed dataset, we benchmark against methods specifically designed for COVID-19 CT analysis:

- **VIT-COVID Classifier [38]:** A ViT pre-trained on a large-

scale dataset of COVID-19 CT images, designed for binary classification.

- **Progressively Resized 3D-CNN [13]:** A CNN that progressively resizes input volumes to extract multi-scale information, enhancing analysis in volumetric CT images.
- **3D U-Net [2]:** A fully supervised segmentation model trained with voxel-level annotations, providing a direct comparison compared to weakly supervised methods.
- **3D GAN [34]:** A weakly supervised generative model that performs volume-level segmentation without requiring dense voxel-level annotations.

WSI Datasets. For the CAMELYON16 and BRACS datasets, we compare INSIGHT against leading MIL-based methods. To ensure a fair comparison, all methods (including ours) use the UNI encoder [8] for feature extraction:

- **ABMIL [15]:** An attention-based MIL approach that identifies the most informative regions within a slide, commonly used in weakly supervised WSI analysis.
- **CLAM-SB/MB [21]:** A MIL method combining attention mechanisms with clustering to improve localization. CLAM-SB uses a single branch for non-overlapping classes, while CLAM-MB employs multiple branches to target specific classes.
- **TransMIL [35]:** A transformer-based MIL model that captures long-range dependencies within WSIs, enhancing contextual analysis for slide-level classification.

4.4. Quantitative Results

INSIGHT consistently outperformed baseline methods in classification and segmentation tasks across all datasets, demonstrating its adaptability to diverse medical imaging modalities. Performance metrics are reported in Table 1 and Table 2.

Key Results:

- On **CAMELYON16**, INSIGHT achieved a Dice score of 74.6%, outperforming the top competing model by 6.9%. This significant improvement highlights its ability to enhance boundary precision in segmentation tasks.

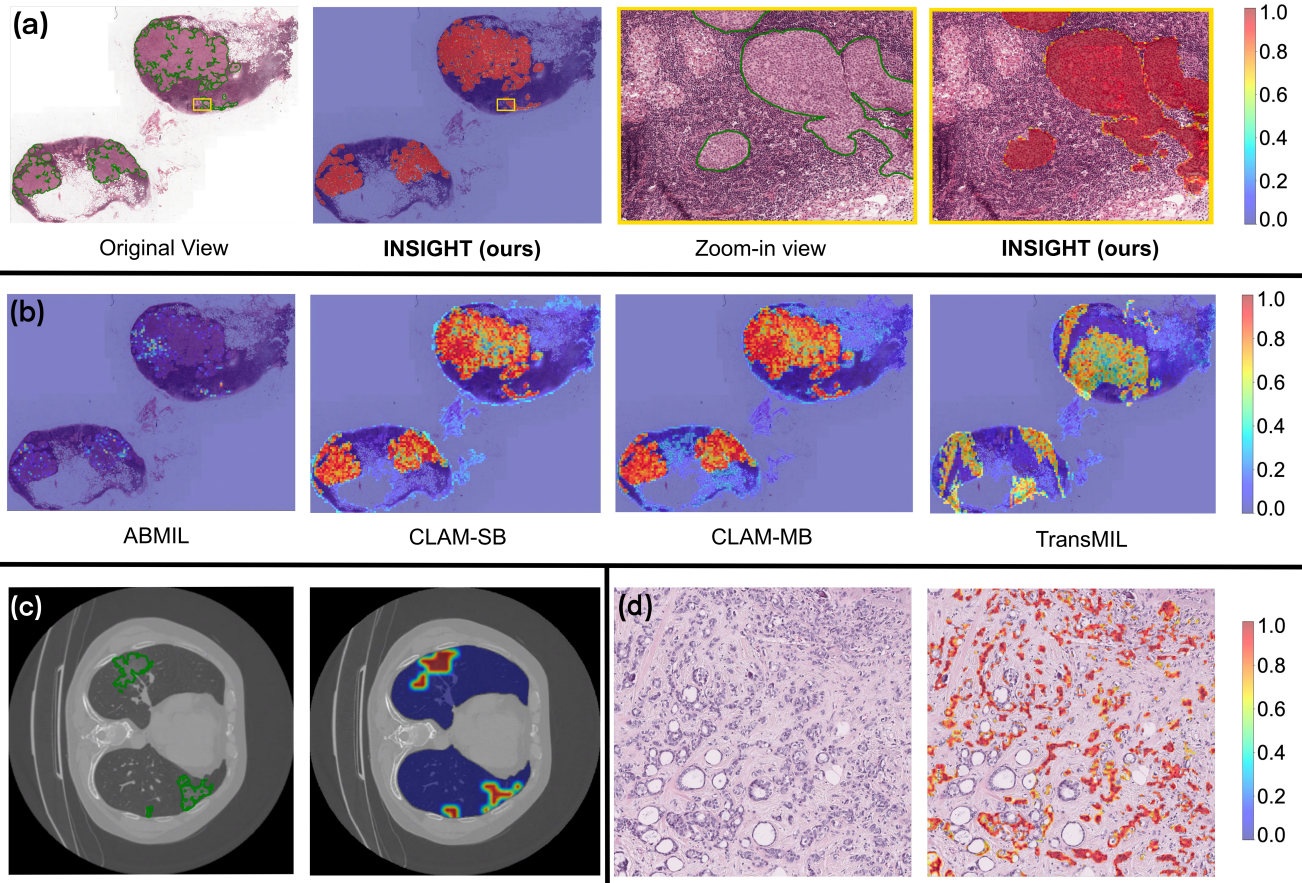


Figure 3. Qualitative comparison of heatmaps generated by INSIGHT (ours) and baseline methods. For CAMELYON16, we compare lesion detection heatmaps generated by (a) our INSIGHT model and (b) the baseline methods. Additionally, we present (c) heatmaps for MosMed and (d) heatmaps for BRACS. Ground-truth areas are outlined in green. Note that BRACS does not provide detailed annotations, so ground truth is not displayed in panel (d). Additional visualizations can be found in the Appendix (Sec. A) for further reference.

- On **BRACS**, INSIGHT demonstrated strong multi-label classification performance, achieving AUC improvements of 3.3% for both ADH and FEA subtyping. This showcases its effectiveness in distinguishing subtle tissue variations critical for breast carcinoma subtype classification.
- On **MosMed**, INSIGHT achieved a classification AUC of 96.2%, nearly 5% higher than the best baseline, underscoring its robustness in volumetric CT analysis for COVID-19 detection.

INSIGHT’s superior performance is attributed to three key architectural innovations:

Spatial Embedding. By retaining spatial resolution during feature extraction, INSIGHT produces feature maps of $16 \times 16 \times 1024$ for CT and $14 \times 14 \times 1024$ for WSIs, preserving diagnostically meaningful spatial structures. In contrast, baseline methods reduce feature maps to $1 \times 1 \times 1024$ vectors via pooling, discarding fine-grained spatial information. This capability enables INSIGHT to detect small but critical

patterns, particularly in datasets like BRACS, where distinct subtypes may co-exist within a single slide.

Adjacent Context Focus. INSIGHT’s context module captures localized dependencies through larger convolutional filters, avoiding the noise introduced by global self-attention mechanisms. This focus on adjacent spatial relationships is particularly effective for multi-label datasets like BRACS, where lesion subtypes often appear in close proximity.

Broader Foreground Activation Consideration. Unlike conventional MIL-based models that focus only on the top k patches, INSIGHT’s smooth pooling method considers all relevant foreground activations above a threshold. This approach preserves finer boundary details, significantly enhancing segmentation accuracy. For example, on CAMELYON16, this broader activation inclusion contributed to its 6.9% Dice score improvement.

INSIGHT’s performance improvements are further supported by qualitative results (Fig. 3) and ablation studies

Table 3. Ablation study results on the MosMed, CAMELYON16, and BRACS datasets. INSIGHT performance is shown with different configurations of CS (Context Suppression), SM (SmoothMax), and Rg (Regularizer).

Config			MosMed [24]		CAMELYON16 [18]		BRACS [1]			
CS	SM	Rg	AUC	Dice(%)	AUC	Dice(%)	ADH	FEA	DCIS	Invasive
✗	✗	✗	0.968±0.016	34.9±15.2	0.992	25.5±16.3	0.741	0.509	0.764	0.993
✓	✗	✗	0.947±0.032	36.9±15.7	0.982	42.1±21.4	0.733	0.507	0.799	0.998
✓	✓	✗	0.955±0.026	42.9±15.4	0.969	76.7±15.7	0.728	0.767	0.834	0.999
✓	✓	✓	0.962±0.012	42.7±15.3	0.990	74.6±19.1	0.734	0.790	0.837	0.999

(Sec. 4.6), demonstrating the critical role of its architectural innovations in achieving state-of-the-art results.

4.5. Qualitative Analysis

We visualize and compare heatmaps generated by INSIGHT and baseline methods in Fig. 3. Unlike baseline methods, which often rely on post-hoc adjustments, INSIGHT directly integrates interpretability into its architecture, mapping each patch’s probability to the heatmap. This eliminates the need for additional calibration steps, producing well-calibrated, fine-grained heatmaps that effectively highlight diagnostically significant regions. Additional visualizations are provided in Appendix A, which further illustrate the superior interpretability and precision of INSIGHT’s heatmaps across both WSIs and CT datasets.

WSI Heatmap Comparisons:

- **INSIGHT:** The heatmaps generated by INSIGHT accurately capture subtle structures and ensure comprehensive coverage of ground-truth areas. Zoomed-in views reveal precise delineation of lesion boundaries, showcasing INSIGHT’s ability to localize regions critical for diagnosis. Ground-truth areas exhibit high activation values, reflecting the model’s robustness in spatially aligning predictions with annotations.
- **ABMIL:** Heatmaps from ABMIL frequently produce false negatives, detecting only a limited number of patches and failing to capture a holistic view of lesion regions. This lack of coverage diminishes its diagnostic utility, particularly in cases with subtle abnormalities.
- **CLAM:** While CLAM’s heatmaps overlap with ground-truth regions, they often exhibit poor calibration, with significant portions of the lesion areas showing low activation values. This leads to suboptimal localization, especially for boundaries.
- **TransMIL:** Heatmaps generated by TransMIL suffer from numerous false positives, marking non-lesion areas as relevant. This overactivation reduces diagnostic precision and makes the results less interpretable for clinical use.

CT Heatmap Comparisons: INSIGHT demonstrates strong generalization across modalities, accurately highlight-

ing infected regions in CT volumes. This is particularly evident in MosMed, where INSIGHT’s heatmaps precisely localize areas of COVID-19 infection with minimal false positives or negatives. These findings underscore INSIGHT’s versatility and robustness compared to baseline methods.

4.6. Ablation Studies

To validate the effectiveness of INSIGHT’s architectural components, we perform an ablation study analyzing three key innovations: context suppression, SmoothMax pooling, and regularization. Results for the MosMed, CAMELYON16, and BRACS datasets are shown in Table 3. The study evaluates both binary (MosMed, CAMELYON16) and multi-label (BRACS) tasks, revealing how each component contributes to classification and segmentation performance.

Key Ablation Study Findings:

- **Context Suppression:** Adding context suppression (Row 2) improves Dice scores across all datasets, with a notable gain of 16.6 on CAMELYON16. This enhancement highlights the module’s ability to improve spatial alignment between predictions and ground truth by selectively focusing on relevant regions while suppressing background noise. However, context suppression alone does not maximize AUC, indicating that spatial coherence alone is insufficient for capturing the discriminative features required for optimal classification performance.
- **SmoothMax Pooling:** Incorporating SmoothMax pooling alongside context suppression (Row 3) results in a substantial Dice score increase of 34.6 on CAMELYON16, emphasizing its role in refining lesion boundaries by leveraging all pixel-level activations. This pooling strategy improves the model’s ability to capture nuanced spatial details, enhancing boundary precision. However, SmoothMax pooling slightly reduces AUC for binary tasks, likely due to the softened decision boundaries introduced by spatial averaging, which may blur class distinctions.
- **Regularization:** Adding regularization (Row 4) improves both AUC and Dice scores across datasets, stabilizing AUC performance in MosMed and enhancing robustness in BRACS. Spectral decoupling mitigates overfitting in single-label tasks like MosMed, ensuring broader feature

utilization and improved generalization. For multi-label tasks like BRACS, label smoothing particularly benefits smaller classes such as ADH and FEA, improving classification consistency across imbalanced distributions.

5. Discussion

Accurately detecting and interpreting disease-related regions in medical imaging remains a critical challenge, particularly when only image-level annotations are available. INSIGHT addresses this gap by achieving state-of-the-art performance in both classification and segmentation tasks across CT volumes and WSIs using *only* image-level labels. This capability is transformative, as it aligns with real-world clinical workflows where physicians rarely annotate images at the pixel or voxel level. By enabling the use of far larger datasets for training, INSIGHT unlocks the potential for scalable and efficient medical imaging solutions.

INSIGHT’s architectural innovations—its detection and context modules—allow it to combine local feature analysis with contextual understanding, generating interpretable and well-calibrated heatmaps. These heatmaps not only enhance diagnostic transparency but also reduce reliance on extensive pixel-level annotations. Such capabilities could accelerate physician annotations [30], allowing clinicians to correct heatmaps rather than annotate from scratch, thereby streamlining annotation workflows where pixel-level labels are required.

Foundation Models and Future Potential. For CT scans, we employed DINOv2 pre-trained on ImageNet due to the absence of publicly available radiology-specific pre-trained models. While this approach yielded strong results, we anticipate further improvements with embeddings tailored to radiology data, which could better capture salient features in CT scans. Similarly, for WSIs, we used UNI, one of the first foundation models in pathology. However, newer and more powerful models, such as Virchow [41], have recently emerged. Leveraging these advanced models for feature extraction could significantly enhance INSIGHT’s performance. Unfortunately, due to computational constraints and the recent public release of these models, we were unable to perform a comparative analysis. Future work will explore integrating these cutting-edge foundation models into INSIGHT to fully harness their potential.

Broader Applicability and Limitations. While INSIGHT has been validated on CT and WSI data, its applicability to other imaging modalities, such as MRI and ultrasound, remains unexplored. In principle, INSIGHT’s architecture should generalize well to these modalities due to its ability to process spatially embedded features and generate interpretable outputs. However, a significant barrier to extending

INSIGHT lies in the scarcity of publicly available datasets for these modalities. Future work will focus on identifying or curating appropriate datasets to evaluate INSIGHT’s generalizability and performance across a broader range of imaging modalities.

6. Conclusion

INSIGHT represents a significant advancement in weakly supervised medical imaging, demonstrating robust performance across diverse tasks and modalities. By effectively leveraging image-level labels, integrating interpretability directly into its architecture, and providing fine-grained diagnostic insights, INSIGHT lays the foundation for scalable and clinically relevant AI solutions. Future efforts will aim to enhance its capabilities with advanced foundation models and extend its applicability to additional imaging modalities, furthering its impact on medical imaging research and practice.

Acknowledgments. This work was supported in part by NSF award #2326491. The views and conclusions contained herein are those of the authors and should not be interpreted as the official policies or endorsements of any sponsor. We thank Jhair Gallardo and Shikhar Srivastava for their comments on early drafts.

References

- [1] Nadia Brancati, Anna Maria Anniciello, Pushpak Pati, Daniel Riccio, Giosuè Scognamiglio, Guillaume Jaume, Giuseppe De Pietro, Maurizio Di Bonito, Antonio Foncubierto, Gerardo Botti, Maria Gabrani, Florinda Feroce, and Maria Frucci. Bracs: A dataset for breast carcinoma subtyping in h&e histology images, 2021. 4, 5, 7
- [2] Keno K. Bresslem, Stefan M. Niehues, Bernd Hamm, Marcus R. Makowski, Janis L. Vahldiek, and Lisa C. Adams. 3d u-net for segmentation of covid-19 associated pulmonary infiltrates using transfer learning: State-of-the-art results on affordable hardware, 2021. 5
- [3] Gabriele Campanella, Matthew G Hanna, Luke Geneslaw, Allen Mirafior, Vitor Werneck Krauss Silva, Klaus J Busam, Edi Brogi, Victor E Reuter, David S Klimstra, and Thomas J Fuchs. Clinical-grade computational pathology using weakly supervised deep learning on whole slide images. *Nature medicine*, 2019. 1, 2
- [4] Marc-André Carbonneau, Veronika Cheplygina, Eric Granger, and Ghyslain Gagnon. Multiple instance learning: A survey of problem characteristics and applications. *Pattern Recognition*, 2018. 2
- [5] Adam Casson, Siqi Liu, Ran A Godrich, Hamed Aghdam, Brandon Rothrock, Kasper Malfroid, Christopher Kanan, and Thomas Fuchs. Joint breast neoplasm detection and subtyping using multi-resolution network trained on large-scale h&e whole slide images with weak labels. In *Medical Imaging with Deep Learning*, 2024. 1, 2

- [6] Runsheng Chang, Shouliang Qi, Yanan Wu, Qiyuan Song, Yong Yue, Xiaoye Zhang, Yubao Guan, and Wei Qian. Deep multiple instance learning for predicting chemotherapy response in non-small cell lung cancer using pretreatment ct images. *Scientific Reports*, 2022. 1, 2
- [7] Liang-Chieh Chen, George Papandreou, Iasonas Kokkinos, Kevin Murphy, and Alan L. Yuille. Deeplab: Semantic image segmentation with deep convolutional nets, atrous convolution, and fully connected crfs, 2017. 2
- [8] Richard J Chen, Tong Ding, Ming Y Lu, Drew FK Williamson, Guillaume Jaume, Bowen Chen, Andrew Zhang, Daniel Shao, Andrew H Song, Muhammad Shaban, et al. Towards a general-purpose foundation model for computational pathology. *Nature Medicine*, 2024. 3, 5
- [9] Precious Chikontwe, Marcel Luna, Min Kang, Kyung-Soo Hong, Jae-Ho Ahn, and Sang Hyun Park. Dual attention multiple instance learning with unsupervised complementary loss for covid-19 screening. *Medical Image Analysis*, 72: 102105, 2021. 3
- [10] Joseph Paul Cohen, Paul Bertin, and Vincent Frappier. Chester: A web delivered locally computed chest x-ray disease prediction system, 2020. 2
- [11] Pierre Courtiol, Eric W. Tramel, Marc Sanselme, and Gilles Wainrib. Classification and disease localization in histopathology using only global labels: A weakly-supervised approach, 2020. 3
- [12] Alexey Dosovitskiy, Lucas Beyer, Alexander Kolesnikov, Dirk Weissenborn, Xiaohua Zhai, Thomas Unterthiner, Mostafa Dehghani, Matthias Minderer, Georg Heigold, Sylvain Gelly, Jakob Uszkoreit, and Neil Houlsby. An image is worth 16x16 words: Transformers for image recognition at scale, 2021. 3
- [13] Md. Kamrul Hasan, Md. Tasnim Jawad, Kazi Nasim Imtiaz Hasan, Sajal Basak Partha, Md. Masum Al Masba, and Shumit Saha. Covid-19 identification from volumetric chest ct scans using a progressively resized 3d-cnn incorporating segmentation, augmentation, and class-rebalancing, 2021. 5
- [14] Julia Hofmanning, Florian Prayer, Jianning Pan, et al. Automatic lung segmentation in routine imaging is primarily a data diversity problem, not a methodology problem. *European Radiology Experimental*, 4(1):50, 2020. 4
- [15] Maximilian Ilse, Jakub M. Tomczak, and Max Welling. Attention-based deep multiple instance learning, 2018. 5
- [16] Issam Laradji, Pau Rodriguez, Oscar Manas, Keegan Lensink, Marco Law, Lironne Kurzman, William Parker, David Vazquez, and Derek Nowrouzezahrai. A weakly supervised consistency-based learning method for covid-19 segmentation in ct images. *arXiv preprint arXiv:2007.02180*, 2020. 2
- [17] Tiancheng Lin, Yuanfan Guo, Yi Xu, and Chang-Wen Chen. Identifying key factors in multi-instance learning for whole-slide pathological images: Designing assumption-guided feature extractor. *SSRN Electronic Journal*, 2022. Available at SSRN: <https://ssrn.com/abstract=4230902> or <http://dx.doi.org/10.2139/ssrn.4230902>. 3
- [18] Geert Litjens, Peter Bandi, Babak Ehteshami Bejnordi, Olaf Geessink, Maschenka Balkenhol, Peter Bult, Alma Halilovic, Meyke Hermesen, Ronald van de Loo, Rob Vogels, Quirine F Manson, Nikolas Stathonikos, Alex Baidoshvili, Paul van Diest, Casper Wauters, Michel van Dijk, and Jeroen van der Laak. 1399 h&e-stained sentinel lymph node sections of breast cancer patients: the camelyon dataset. *Gigascience*, 7(6):giy065, 2018. 4, 5, 7
- [19] Xiaoming Liu, Quan Yuan, Yaozong Gao, Kelei He, Shuo Wang, Xiao Tang, Jinshan Tang, and Dinggang Shen. Weakly supervised segmentation of covid19 infection with scribble annotation on ct images. *Pattern Recognition*, 122:108341, 2022. 2
- [20] Fangfang Lu, Zhihao Zhang, Tianxiang Liu, Chi Tang, Hualin Bai, Guangtao Zhai, Jingjing Chen, and Xiaoxin Wu. A weakly supervised inpainting-based learning method for lung ct image segmentation. *Pattern Recognition*, 144:109861, 2023. 2
- [21] Ming Y Lu, Drew FK Williamson, Tiffany Y Chen, Richard J Chen, Matteo Barbieri, and Faisal Mahmood. Data-efficient and weakly supervised computational pathology on whole-slide images. *Nature biomedical engineering*, 5(6):555–570, 2021. 4, 5
- [22] Chris J Maddison, Andriy Mnih, and Yee Whye Teh. The concrete distribution: A continuous relaxation of discrete random variables. *arXiv preprint arXiv:1611.00712*, 2016. 4
- [23] Usman Mahmood, Robik Shrestha, David DB Bates, Lorenzo Mannelli, Giuseppe Corrias, Yusuf Erdi, and Christopher Kanan. Detecting spurious correlations with sanity tests for artificial intelligence guided radiology systems. *Frontiers in Digital Health*, 2021. 1
- [24] S. P. Morozov, A. E. Andreychenko, N. A. Pavlov, A. V. Vladzimirskyy, N. V. Ledikhova, V. A. Gombolevskiy, I. A. Blokhin, P. B. Gelezhe, A. V. Gonchar, and V. Yu. Chernina. Mosmeddata: Chest ct scans with covid-19 related findings dataset, 2020. 4, 7
- [25] Omar S. M. El Nahhas, Marko van Treeck, Georg Wölflein, Michaela Unger, Marta Ligerio, Tim Lenz, Sophia J. Wagner, Katherine J. Hewitt, Firas Khader, Sebastian Foersch, Daniel Truhn, and Jakob Nikolas Kather. From whole-slide image to biomarker prediction: A protocol for end-to-end deep learning in computational pathology, 2023. 2
- [26] Maxime Oquab, Timothée Darcet, Théo Moutakanni, Huy Vo, Marc Szafranec, Vasil Khalidov, Pierre Fernandez, Daniel Haziza, Francisco Massa, Alaaeldin El-Nouby, Mahmoud Assran, Nicolas Ballas, Wojciech Galuba, Russell Howes, Po-Yao Huang, Shang-Wen Li, Ishan Misra, Michael Rabbat, Vasu Sharma, Gabriel Synnaeve, Hu Xu, Hervé Jegou, Julien Mairal, Patrick Labatut, Armand Joulin, and Piotr Bojanowski. Dinov2: Learning robust visual features without supervision, 2024. 3
- [27] Nobuyuki Otsu. A threshold selection method from gray-level histograms. *IEEE Transactions on Systems, Man, and Cybernetics*, 9(1):62–66, 1979. 4
- [28] Pushpak Pati, Guillaume Jaume, Zeineb Ayadi, Kevin Thandiackal, Behzad Bozorgtabar, Maria Gabrani, and Orcun Goksel. Weakly supervised joint whole-slide segmentation and classification in prostate cancer, 2023. 2
- [29] Joona Pohjonen, Carolin Stürenberg, Antti Rannikko, Tuomas Mirtti, and Esa Pitkänen. Spectral decoupling for training

- transferable neural networks in medical imaging. *Isience*, 2022. 4
- [30] Patricia Raciti, Jillian Sue, Rodrigo Ceballos, Ran Godrich, Jeremy D Kunz, Supriya Kapur, Victor Reuter, Leo Grady, Christopher Kanan, David S Klimstra, et al. Novel artificial intelligence system increases the detection of prostate cancer in whole slide images of core needle biopsies. *Modern Pathology*, 2020. 8
- [31] Olaf Ronneberger, Philipp Fischer, and Thomas Brox. U-net: Convolutional networks for biomedical image segmentation, 2015. 2
- [32] Anindo Saha, Fakrul I. Tushar, Khrystyna Faryna, Vincent M. D’Anniballe, Rui Hou, Maciej A. Mazurowski, Geoffrey D. Rubin, and Joseph Y. Lo. Weakly supervised 3d classification of chest ct using aggregated multi-resolution deep segmentation features. In *Medical Imaging 2020: Computer-Aided Diagnosis*. SPIE, 2020. 2
- [33] Ramprasaath R. Selvaraju, Michael Cogswell, Abhishek Das, Ramakrishna Vedantam, Devi Parikh, and Dhruv Batra. Grad-cam: Visual explanations from deep networks via gradient-based localization. *International Journal of Computer Vision*, 2019. 1, 2, 3
- [34] Sepideh Shabani, Mahdi Homayounfar, Vishal Vardhanabhuti, Mohammad Amin Nikouei Mahani, and Mohammad-hadi Koochi-Moghadam. Self-supervised region-aware segmentation of covid-19 ct images using 3d gan and contrastive learning. *Computers in Biology and Medicine*, 149:106033, 2022. 5
- [35] Zhuchen Shao, Hao Bian, Yang Chen, Yifeng Wang, Jian Zhang, Xiangyang Ji, and Yongbing Zhang. Transmil: Transformer based correlated multiple instance learning for whole slide image classification, 2021. 5
- [36] Robik Shrestha, Kushal Kafle, and Christopher Kanan. An investigation of critical issues in bias mitigation techniques. In *WACV*, 2022. 4
- [37] Robik Shrestha, Kushal Kafle, and Christopher Kanan. Occamnets: Mitigating dataset bias by favoring simpler hypotheses. In *ECCV*, 2022. 4
- [38] Fakrul Islam Tushar, Ehsan Abadi, Saman Sotoudeh-Paima, Rafael B. Fricks, Maciej A. Mazurowski, W. Paul Segars, Ehsan Samei, and Joseph Y. Lo. Virtual vs. reality: External validation of covid-19 classifiers using xcat phantoms for chest computed tomography, 2022. 5
- [39] Ashish Vaswani, Noam Shazeer, Niki Parmar, Jakob Uszkoreit, Llion Jones, Aidan N. Gomez, Lukasz Kaiser, and Illia Polosukhin. Attention is all you need, 2023. 3
- [40] Ostap Viniavskyi, Mariia Dobko, and Oles Doboševych. Weakly-supervised segmentation for disease localization in chest x-ray images. In *Artificial Intelligence in Medicine*, pages 249–259. Springer International Publishing, 2020. 3
- [41] Eugene Vorontsov, Alican Bozkurt, Adam Casson, George Shaikovski, Michal Zelechowski, Kristen Severson, Eric Zimmermann, James Hall, Neil Tenenholtz, Nicolo Fusi, et al. A foundation model for clinical-grade computational pathology and rare cancers detection. *Nature medicine*, pages 1–12, 2024. 8
- [42] Weiyi Xie, Colin Jacobs, Jean-Paul Charbonnier, and Bram van Ginneken. Dense regression activation maps for lesion segmentation in ct scans of covid-19 patients. *Medical Image Analysis*, 86:102771, 2023. 3
- [43] Qinghao Ye, Yuan Gao, Weiping Ding, Zhangming Niu, Chengjia Wang, Yinghui Jiang, Minhao Wang, Evandro Fei Fang, Wade Menpes-Smith, Jun Xia, and Guang Yang. Robust weakly supervised learning for covid-19 recognition using multi-center ct images. *Applied Soft Computing*, 116:108291, 2022. 2
- [44] Xin Zhang, Liangxiu Han, Wenyong Zhu, Liang Sun, and Daoqiang Zhang. An explainable 3d residual self-attention deep neural network for joint atrophy localization and alzheimer’s disease diagnosis using structural mri. *IEEE Journal of Biomedical and Health Informatics*, 26(11):5289–5297, 2022. 3
- [45] Bolei Zhou, Aditya Khosla, Agata Lapedriza, Aude Oliva, and Antonio Torralba. Learning deep features for discriminative localization, 2015. 2, 3
- [46] Lingxuan Zhu, Jiahua Pan, Weiming Mou, Longxin Deng, Yinjie Zhu, Yanqing Wang, Gyan Pareek, Elias Hyams, Benedito A Carneiro, Matthew J Hadfield, et al. Harnessing artificial intelligence for prostate cancer management. *Cell Reports Medicine*, 2024. 2

Appendix

A. Qualitative Analysis

We provide additional visualization results (Fig. 4, 5, 6) to further demonstrate INSIGHT’s ability to generate well-calibrated heatmaps that align with diagnostically relevant regions in the Camelyon16 dataset. These visualizations reinforce the interpretability of INSIGHT. Please zoom in to view finer details.

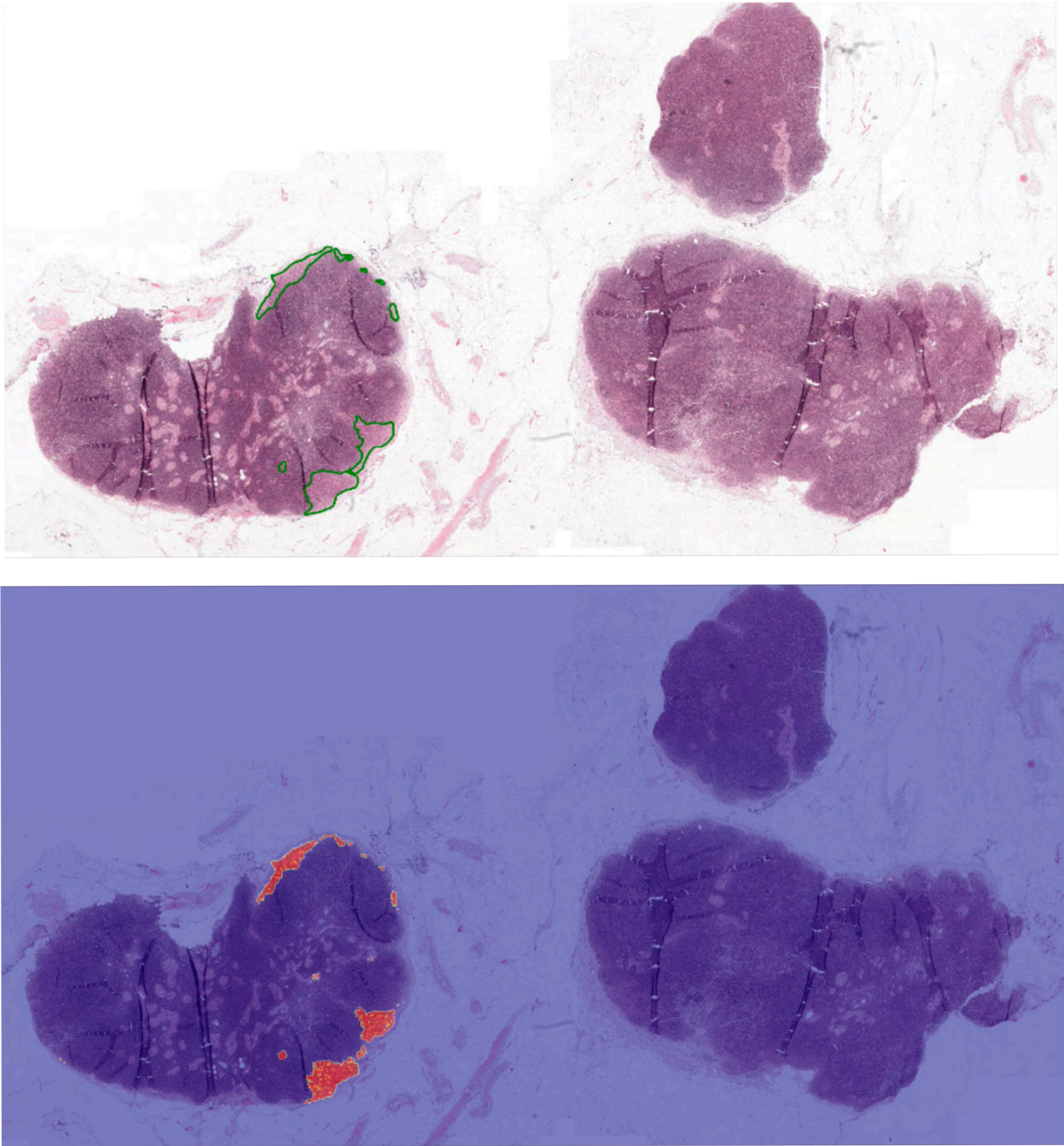


Figure 4. WSI heatmap visualizations generated by INSIGHT. The green outlines on the original image represent ground-truth regions.

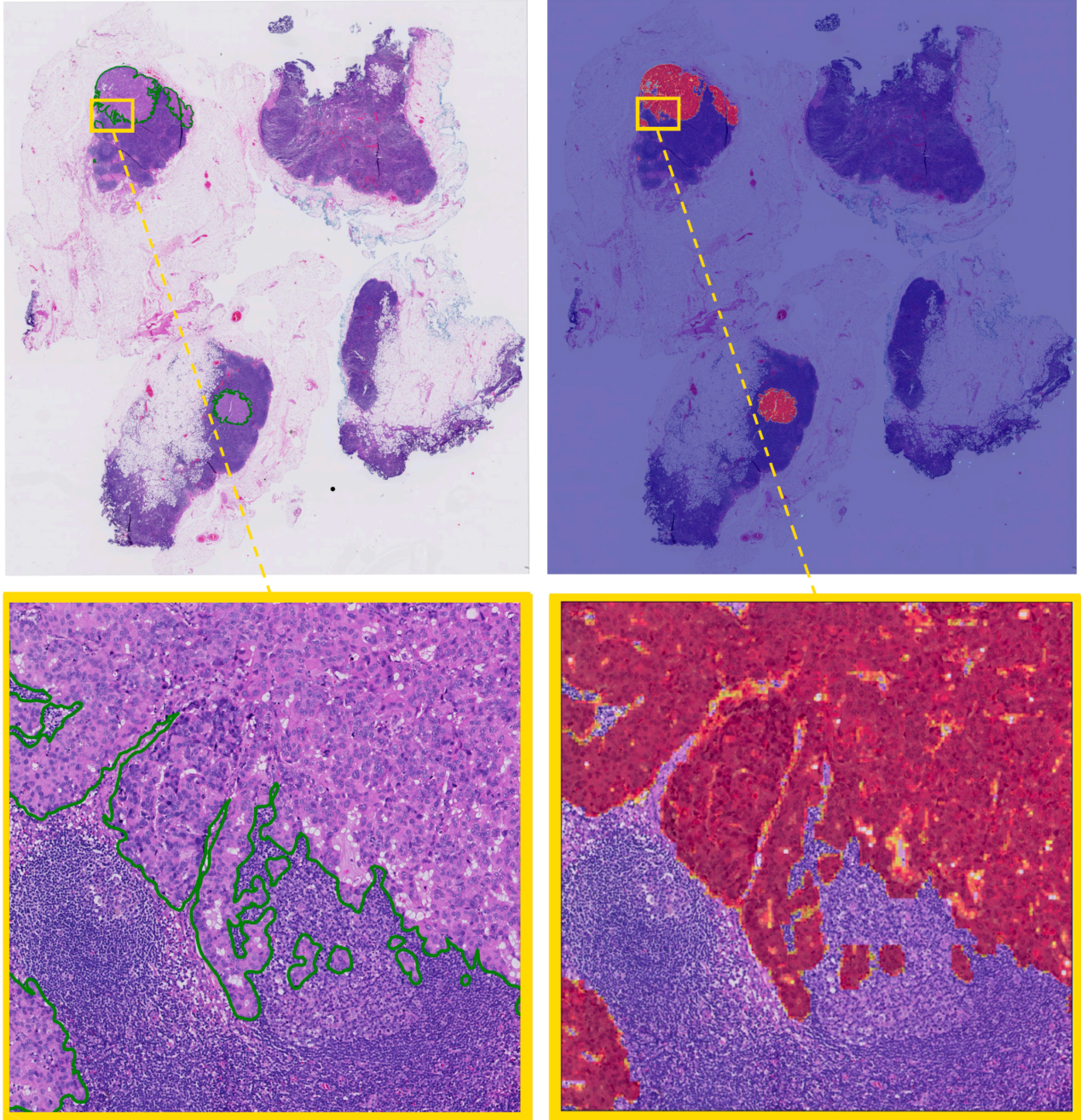


Figure 5. Original histopathology image (left) and the corresponding heatmap generated by INSIGHT (right). The green outlines on the original image represent ground-truth regions. The bottom row provides zoomed-in views of the regions highlighted by yellow boxes.

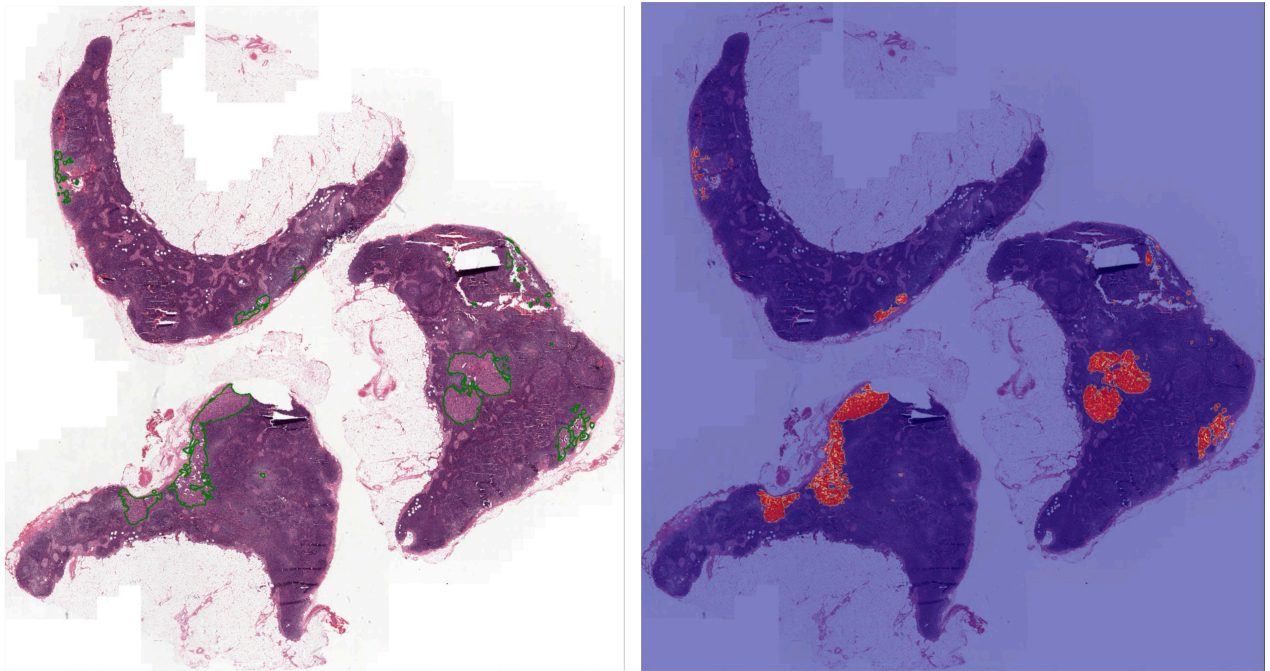


Figure 6. Additional WSI heatmap visualizations generated by INSIGHT. The green outlines represent ground-truth regions.

B. Ablation

INSIGHT retains spatial resolution during the feature extraction process, and the output feature maps preserve spatial structure, resulting in dimensions of $16 \times 16 \times 1024$ for CT slices and $14 \times 14 \times 1024$ for WSI tiles. In contrast, compared methods typically apply a pooling strategy that reduces the feature map to a $1 \times 1 \times 1024$ vector that discards spatial information. To evaluate the effectiveness of our spatial embedding, we conducted an ablation study where the spatial embedding was replaced with a non-spatial one. The results are summarized in Table 4, which highlights the impact of maintaining spatial resolution. Retaining spatial resolution increased the classification AUC by 4.5% and improved the Dice score for segmentation by over 15%. These substantial improvements underscore the critical role of spatial information in histopathological analysis, particularly for segmentation tasks that rely on fine-grained details and spatial continuity to localize regions of interest accurately. Additionally, compared to transformer-based aggregators, which face a quadratic increase in computational cost, INSIGHT leverages its lightweight CNN architecture to achieve a near-linear increase in computation, enabling it to fully capitalize on the benefits of spatial embedding.

Table 4. Ablation study results comparing tensor embeddings and vector embeddings for WSIs on CAMELYON16 dataset. We report AUC for classification, Dice for segmentation, and average time used for generating a heatmap.

Spatial Embedding	AUC	Dice (%)	Runtime (s)
\times	0.945	59.1 ± 24.8	1
\checkmark	0.990	74.6 ± 19.1	33